S1 Experimental

S1.1 Materials

Zinc sulfate heptahydrate ($ZnSO_4 \cdot 7H_2O$), ammonium metavanadate (NH_4VO_3), oxalic acid dihydrate ($H_2C_2O_4 \cdot 2H_2O$) and N-Methylpyrrolidone (NMP) are purchased from Shanghai Aladdin Biochemical Technology Co., Ltd. Commercial zinc foil (30 μm) and commercial copper foil (30 μm) are purchased from Shenghang Metal Materials Co., Ltd. Glass fiber (GF) is purchased from Tianjin EVS Chemical Technology Co., Ltd.

S1.2 Pretreatment of separator

The glass fiber separators are cut into the required size, and then place them in a drying oven. Dry them at 80 °C for 12 h to remove adsorbed water molecules and other volatile impurities, thus avoiding the adverse impacts of residual moisture on the subsequent magnetron sputtering process.

S1.3 Preparation of GF-B-1, GF-B-5, and GF-B-10

The glass-fiber separators are modified via a radio-frequency (RF) magnetron sputtering system (Sputter-100, Beijing Tailong Electronic Co., Ltd.) equipped with a boron target. After the separators is placed into the chamber, the system is evacuated. Meanwhile, the sputtering process flow, including RF power, sputtering time and other process parameters, is preset. When the vacuum level drops below 10^{-5} Pa, high-purity Ar (100%) is introduced as the working gas, and the RF sputtering process commences. The deposition parameters are precisely controlled at 300 W, and sputtering times are respectively set to 1, 5, and 10 min. To ensure a uniform coating, each side of the separator undergoes sputtering treatment in two individual cycles. Once the preset steps are completed, the RF power supply is switched off, the chamber is evacuated to atmospheric pressure, and the modified separator is taken out for subsequent use.

S1.4 Preparation of $NH_4V_4O_{10}$ Cathodes

$NH_4V_4O_{10}$ (NVO) is synthesized following a reported hydrothermal method[1]. First, 1.17 g of NH_4VO_3 is dissolved in 50 mL deionized water at 80 °C and stir for about 10 min until a light-yellow clear solution appear. Then, 1.891 g of $H_2C_2O_4 \cdot 2H_2O$ is added, and stirring continue until

the solution turn dark blue. The mixture is transferred into an 80 mL PTFE-lined autoclave and heat at 140 °C for 48 h. After natural cooling, the product is collected and washed several times by centrifugation with deionized water, followed by drying at 80 °C for 12 h to obtain NVO powder.

For electrode preparation, NVO, Super-P, and PVDF are mixed at a 7:2:1 mass ratio and dry-ground for 15 min. NMP is then added to form a uniform slurry, which is coated onto a 12 mm stainless-steel mesh and dry under vacuum at 80 °C for 10 h. The active-material loading is about 3 mg cm^{-2}.

S2 Material characterization

The electrolyte wettability of different separators is evaluated by measuring the static contact angles of zinc sulfate solution using a contact angle meter (SDC-350KS). X-ray diffraction (XRD, PANalytical, Empyrean 2) is conducted on Zn foils after 50 electrochemical cycles to investigate their surface crystalline orientation and to determine the amount of ZSH by-product during cycling. Scanning electron microscopy (SEM, JEOL, JSM-7610FPlus) and Energy Dispersive Spectrometer (EDS) is employed to investigate the surface morphology of Zn foils after cycles and the separators. The high-resolution micrographs provide direct insight into the evolution of surface features, including dendrite formation，holes and crack, thereby enabling a better understanding of the mechanisms during cycling. X-ray photoelectron spectroscopy (XPS) is employed to characterize the glass-fiber separators and to analyze the boron content as well as its chemical states. Laser confocal microscopy (LCM, LSM700) is employed to examine the surface morphology and roughness of zinc anodes after cycling. The pore size distribution and average pore diameter of the separator were determined by Brunauer-Emmett-Teller (BET) method using a JW-BK200 specific surface area and pore size analyzer.

S3 Electrochemical characterization

All electrochemical tests are carried out by the coin cells (CR2025). Electrochemical performance tests are conducted on 2025-type coin cells, which are assembled using zinc foil as the anode and a 2M $ZnSO_4$ aqueous solution as the electrolyte. Asymmetric cells with different separators are constructed by employing commercial copper foil as the working electrode. To

evaluate electrochemical behavior, coin-type cells are fabricated using zinc foils as the anode together with 2M $ZnSO_4$ aqueous electrolyte. Symmetric cells are further prepared, in which two identical zinc foils act as both working and counter electrodes. In addition, full cells incorporating NVO cathodes are assembled for cycling performance tests of the GF separators. Galvanostatic charge-discharge measurements are carried out on a Neware MIHW-200-160CH testing system at 30 ℃. Electrochemical impedance spectroscopy (EIS) of the symmetric cells is recorded over a frequency window of 0.01-100000 Hz. Symmetric SS||SS cells are assembled using stainless steel as both electrodes, and the ionic conductivity of different separators is evaluated by electrochemical impedance spectroscopy (EIS). Chronoamperometry (CA) is performed under a constant overpotential of −200 mV for 600 s, and Tafel analysis is conducted at a scan rate of 1 mV s^{-1}. All EIS, CA, and Tafel experiments are completed on a CHI660E electrochemical workstation under ambient conditions.

S4 Calculation of ionic conductivity

To determine the ionic conductivity of the separators, SS||SS symmetric cells are assembled and tested by EIS, and the conductivity is calculated according to Eq. (1)[2].

$$\sigma = \frac{L}{RS} \tag{1}$$

where L denotes the separator thickness (μm), S represents the effective electrode contact area (cm^2), and R corresponds to the ohmic bulk resistance obtain from the high-frequency intercept of the Nyquist plots.

S5 Theoretical calculations

Density functional theory (DFT) calculations are carried out using the CASTEP module in Materials Studio. The generalized gradient approximation (GGA) with the Perdew-Burke-Ernzerhof (PBE) functional is adopted to describe the exchange-correlation interactions. The k-point grid is generated based on a k-point separation of 0.07 $Å^{-1}$, and the plane-wave cutoff energy is set to 517 eV. A vacuum region of 20 Å is applied above the slab surface to eliminate interactions between periodic images. During the structural optimization, the bottom layers of each slab model are fixed while the remaining atoms are allowed to fully relax.

The amorphous SiO_2 structure is obtained through geometry optimization and molecular dynamics annealing of crystalline SiO_2. The crystalline phase is first converted into a right-angle unit cell and then expand to a suitable supercell size. A heating-cooling MD process is applied, in which the system is heated to 1996 K and equilibrated for 2000 ps, followed by cooling to 298 K under an NVT ensemble with a time step of 1 fs.

The binding energy is calculated by the following equation:

$E_b = E(total) - E(substrate) - E(Zn)$

Where E(total), E(substrate) and E(Zn) represent the total energy of substrate with Zn, the energy of substrate and zinc atom, respectively.

$E_b' = E(total) - E(substrate) - E(SO_4^{2-})$

Where E(total), E(substrate) and $E(SO_4^{2-})$ represent the total energy of substrate with SO_4^{2-}, the energy of substrate and SO_4^{2-}, respectively.

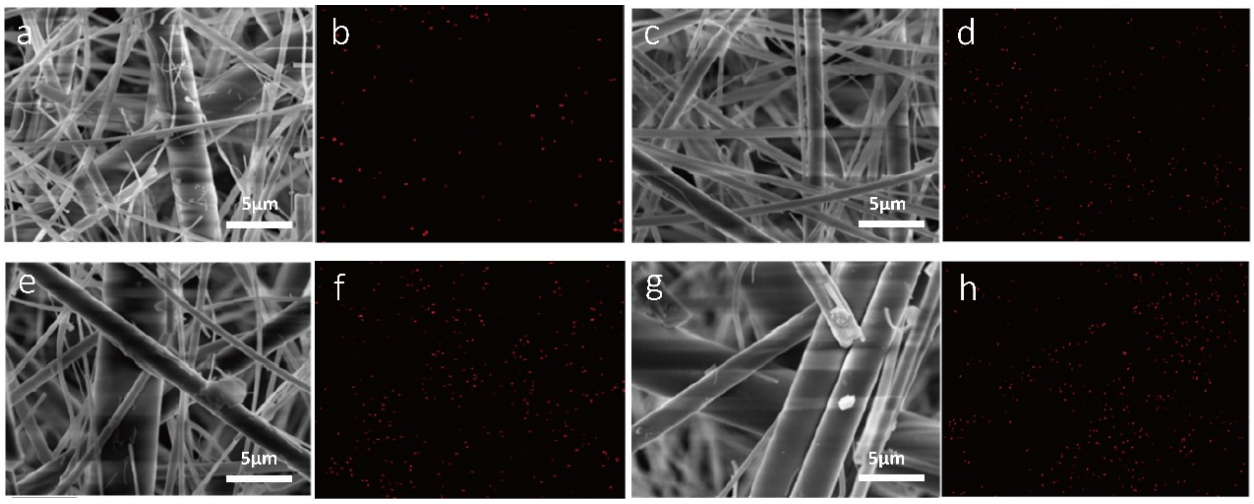

Fig. S1 SEM and EDS of different separators. (a, b) Pristine GF separator: (a) SEM morphology image,(b) corresponding EDS elemental mapping of B element. (c, d) GF-B-1: (c) SEM morphology image, (d) corresponding EDS elemental mapping of B element. (e, f) GF-B-5: (e) SEM morphology image, (f) corresponding EDS elemental mapping of B element. (g, h) GF-B-10: (g) SEM morphology image, (h) corresponding EDS elemental mapping of B element.

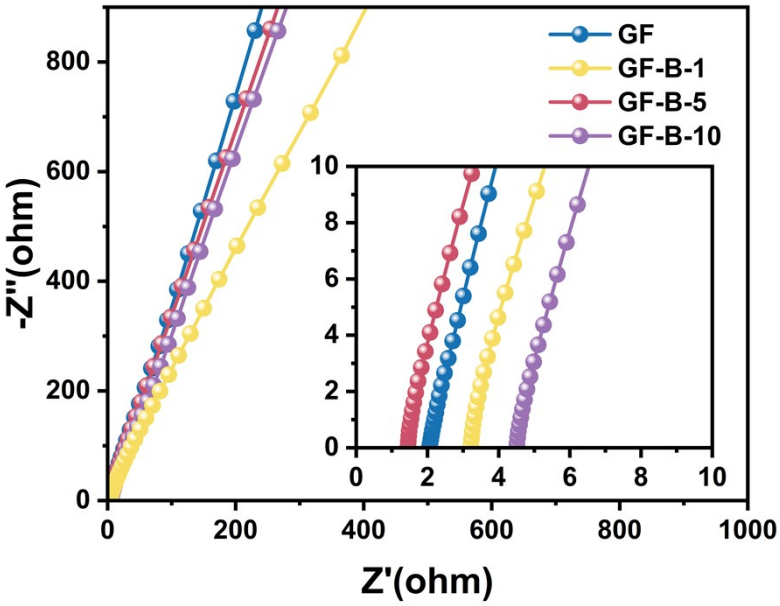

Fig. S2 The ionic conductivity of various separators.

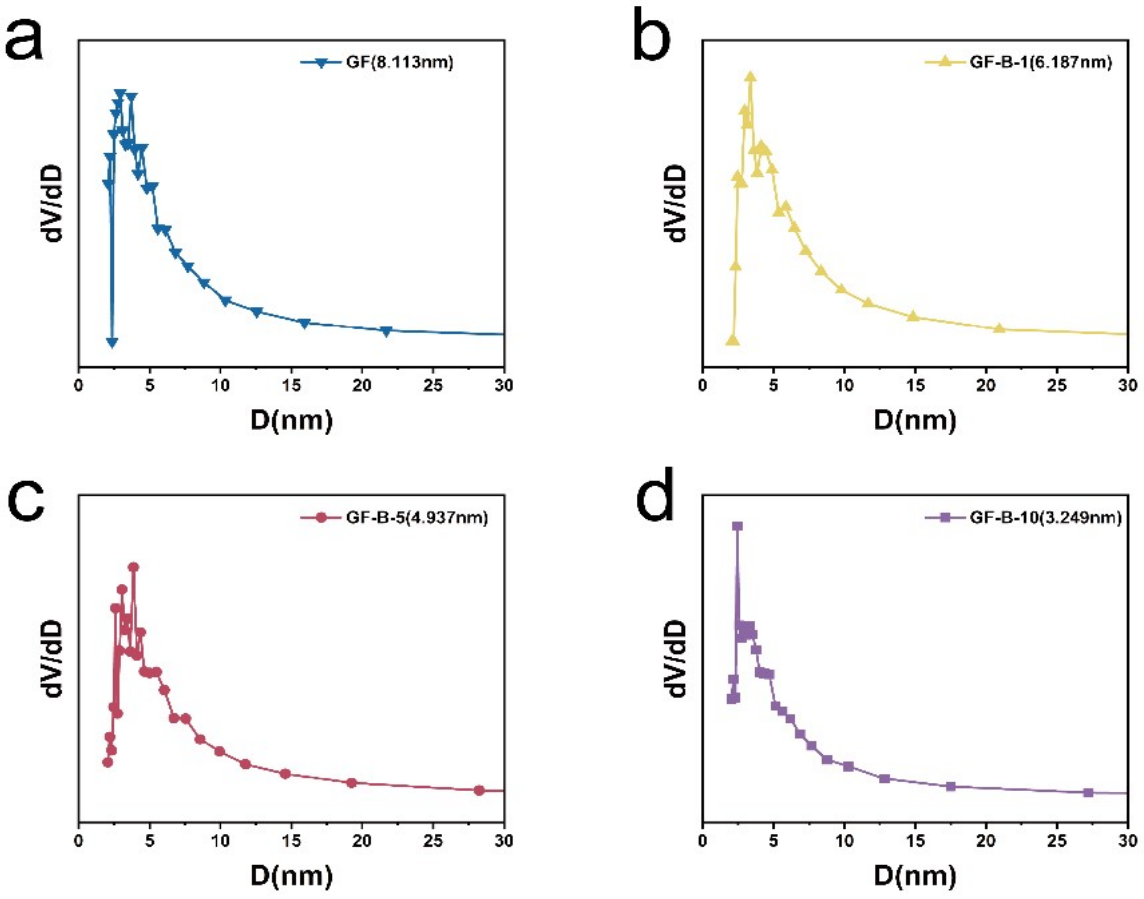

Fig. S3 The pore size distribution of the (a) GF, (b) GF-B-1, (c) GF-B-5 and (d) GF-B-10 separators.

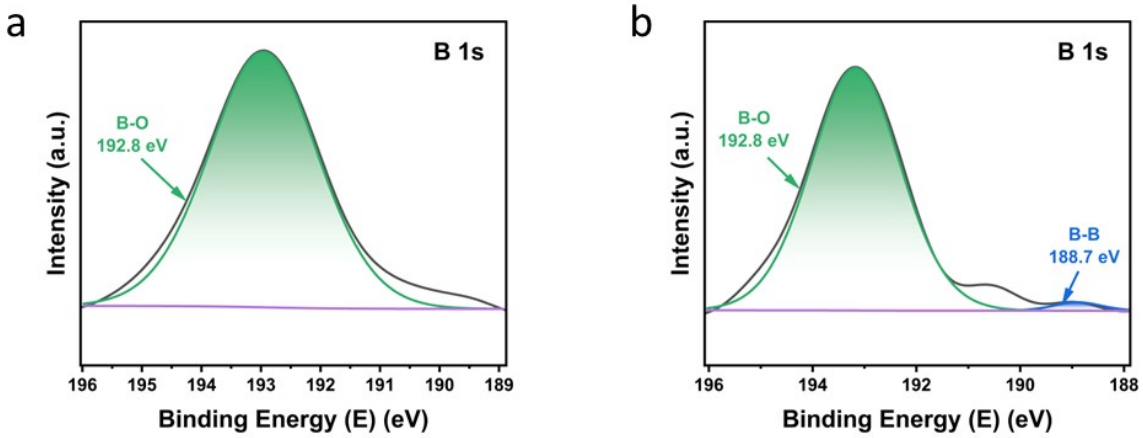

Fig. S4 B 1s XPS spectra of (a) GF-B-1 and (b) GF-B-10 separators.

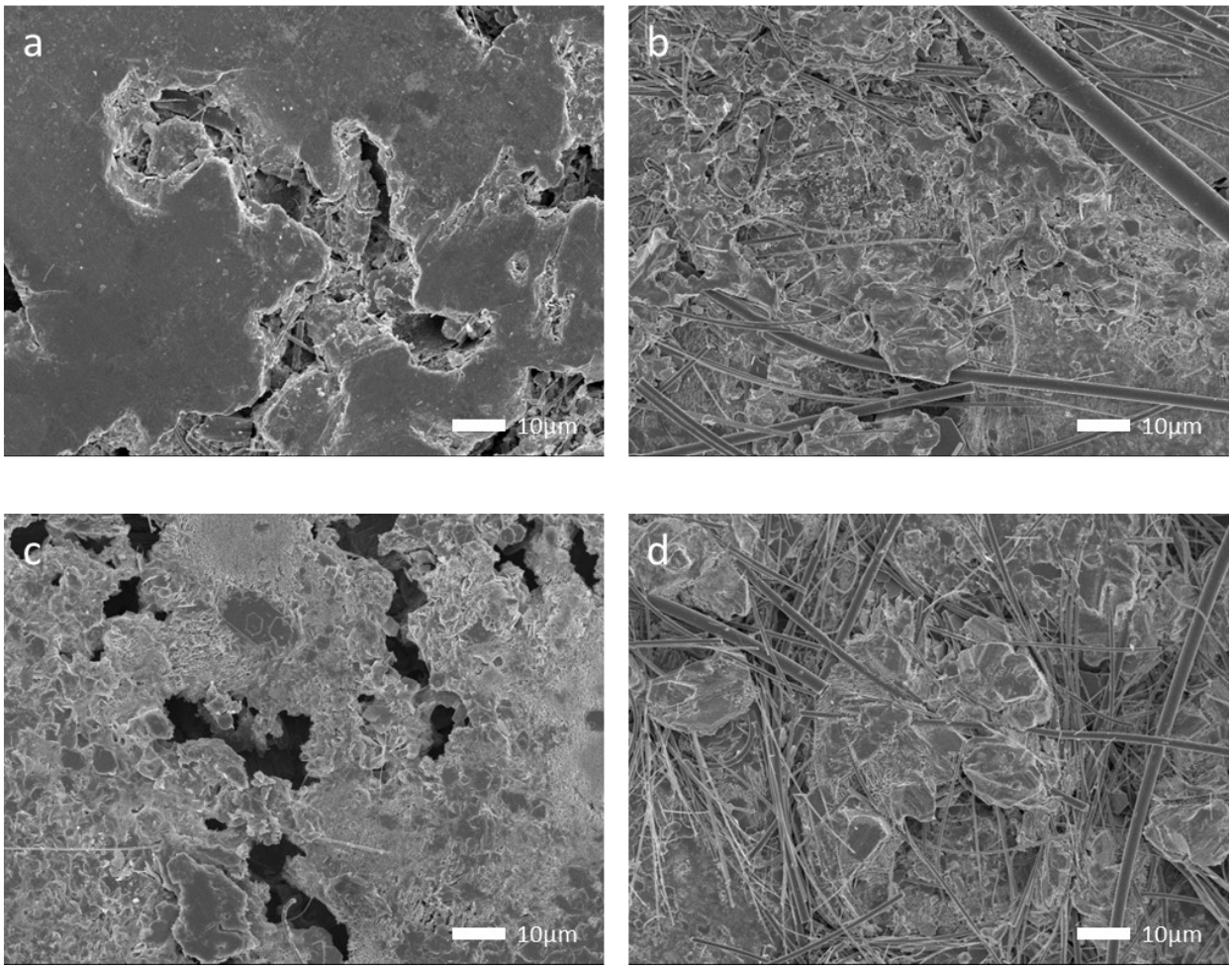

Fig. S5 Reversibility of stripping/plating in Zn||Zn symmetric batteries after cycles at 5 mA cm^{-2} and 1 mAh cm^{-2}. SEM images of Zn anodes: (a) and (b) using GF separator after first cycle, (c) and (d) after 50 cycles.

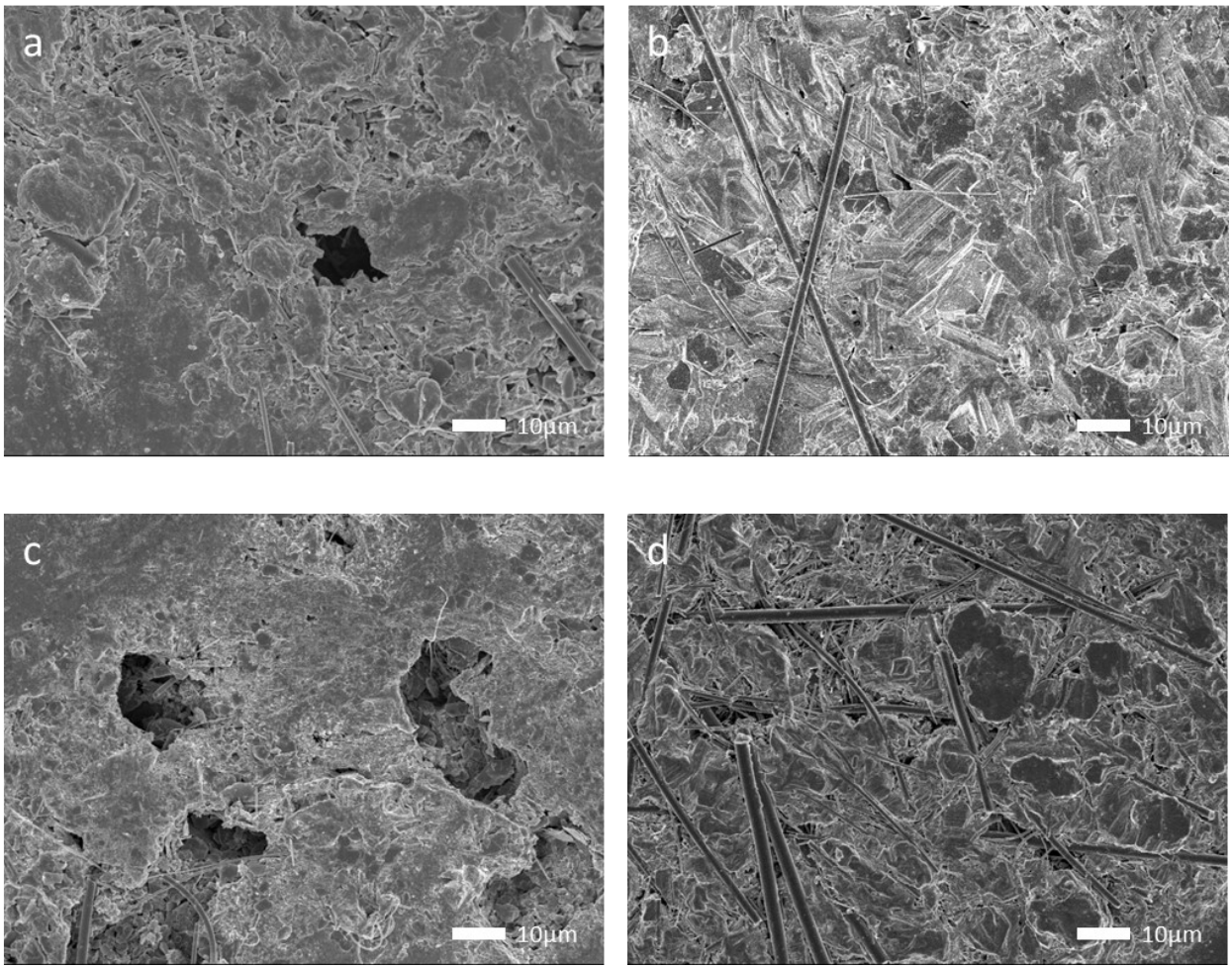

Fig. S6 Reversibility of stripping/plating in Zn||Zn symmetric batteries after cycles at 5 mA cm^{-2} and 1 mAh cm^{-2}. SEM images of Zn anodes: (a) and (b) using GF-B-1 separator after first cycle, (c) and (d) after 50 cycles.

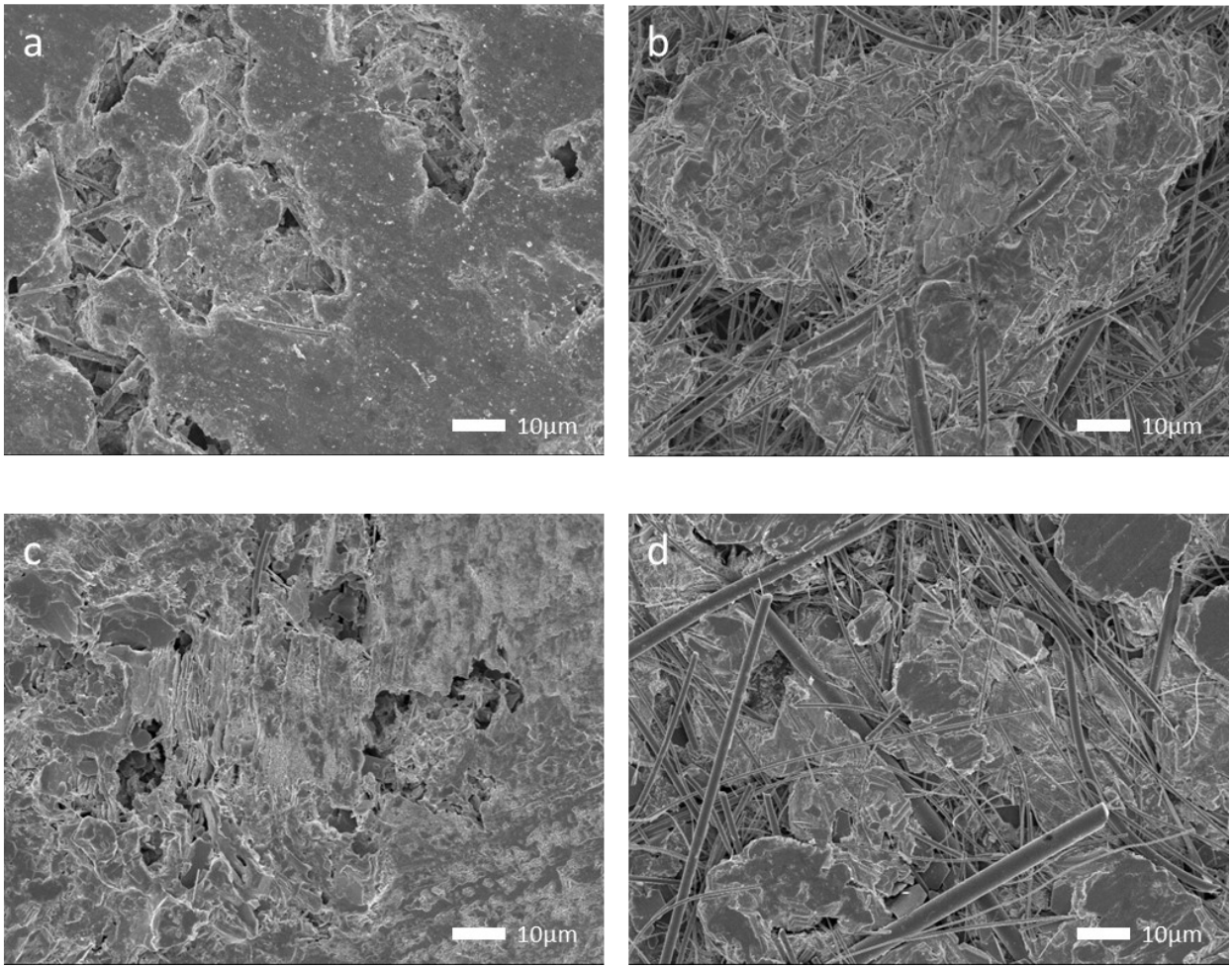

Fig. S7 Reversibility of stripping/plating in Zn||Zn symmetric batteries after cycles at 5 mA cm^{-2} and 1 mAh cm^{-2}. SEM images of Zn anodes: (a) and (b) using GF-B-10 separator after first cycle, (c) and (d) after 50 cycles.

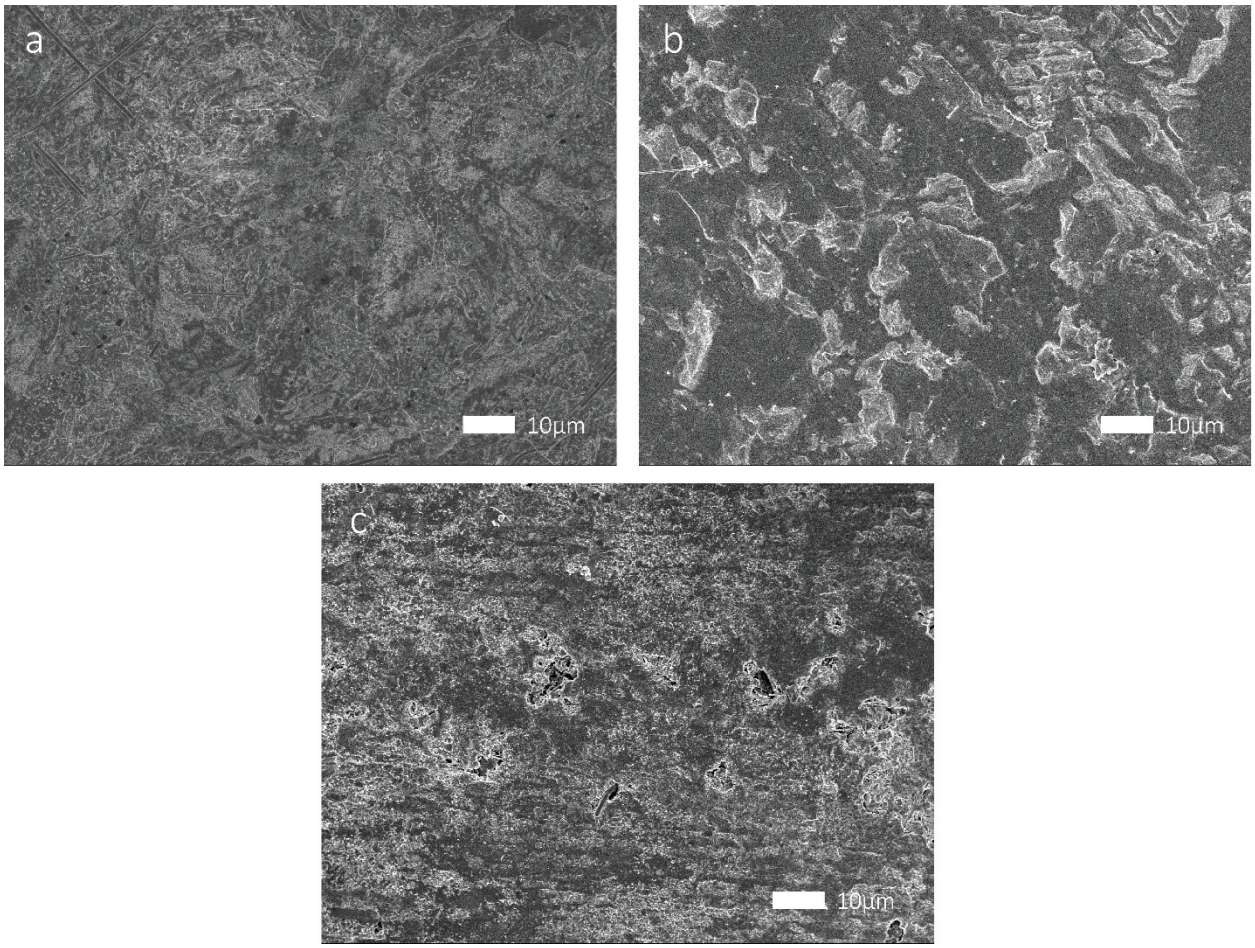

Fig. S8 SEM images of Zn foils with GF-B-5 separator after the first cycle at 5 mA cm^{-2} and 1 mAh cm^{-2}: (a) deposition and (b) stripping side. (c) SEM images of Zn anodes after 50 cycles stripping at 5 mA cm^{-2} and 1 mAh cm^{-2}.

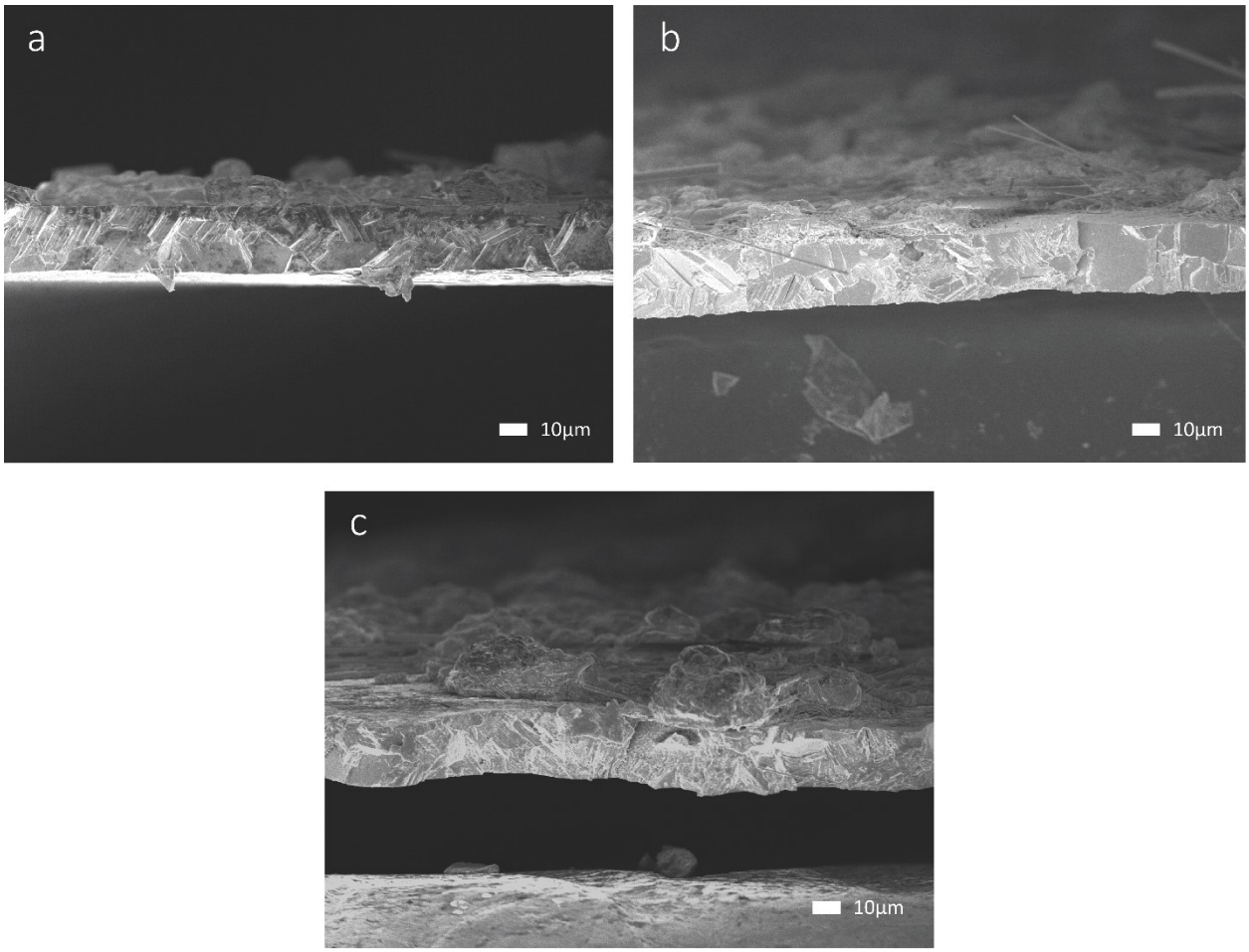

Fig. S9 Cross-sectional SEM images of Zn foils with (a) GF, (b) GF-B-1 and (c) GF-B-10 separators after 50 cycles at 5 mA cm^{-2} and 1 mAh cm^{-2}.

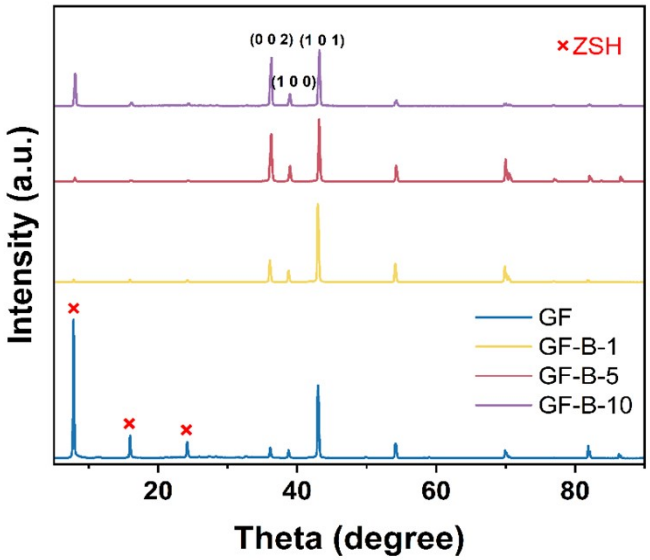

Fig. S10 XRD patterns of zinc anodes from Zn||Zn symmetric cells after 50 cycles at 5 mA cm^{-2} with a capacity of 1 mAh cm^{-2} (4 M $ZnSO_4$ electrolyte).

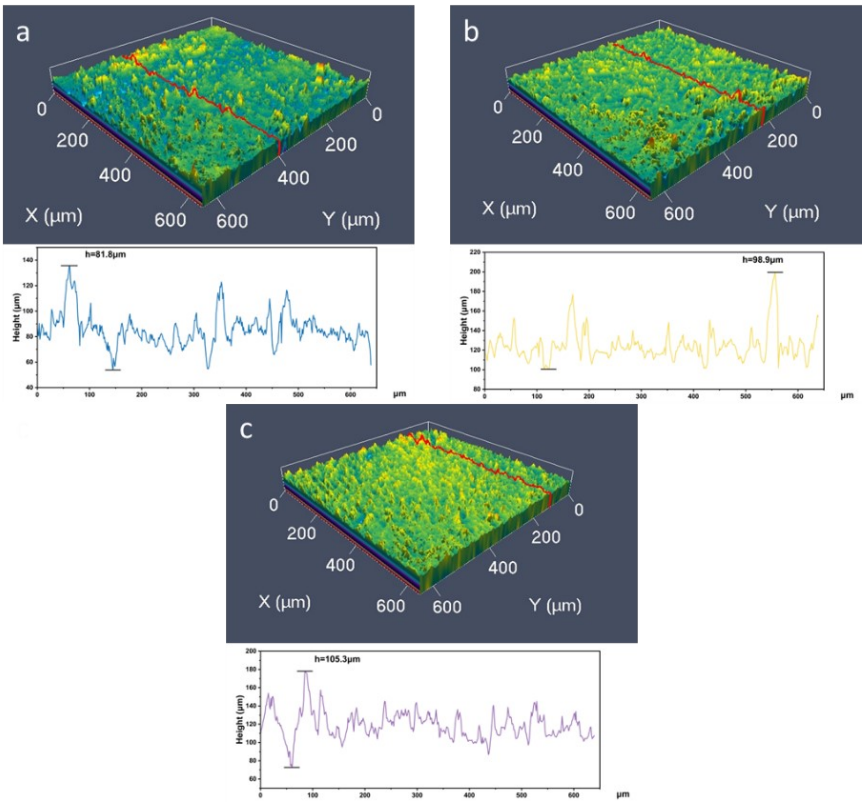

Fig. S11 LCM images of Zn foils after deposition with different separators: (a) GF, (b) GF-B-1, and (c) GF-B-10.

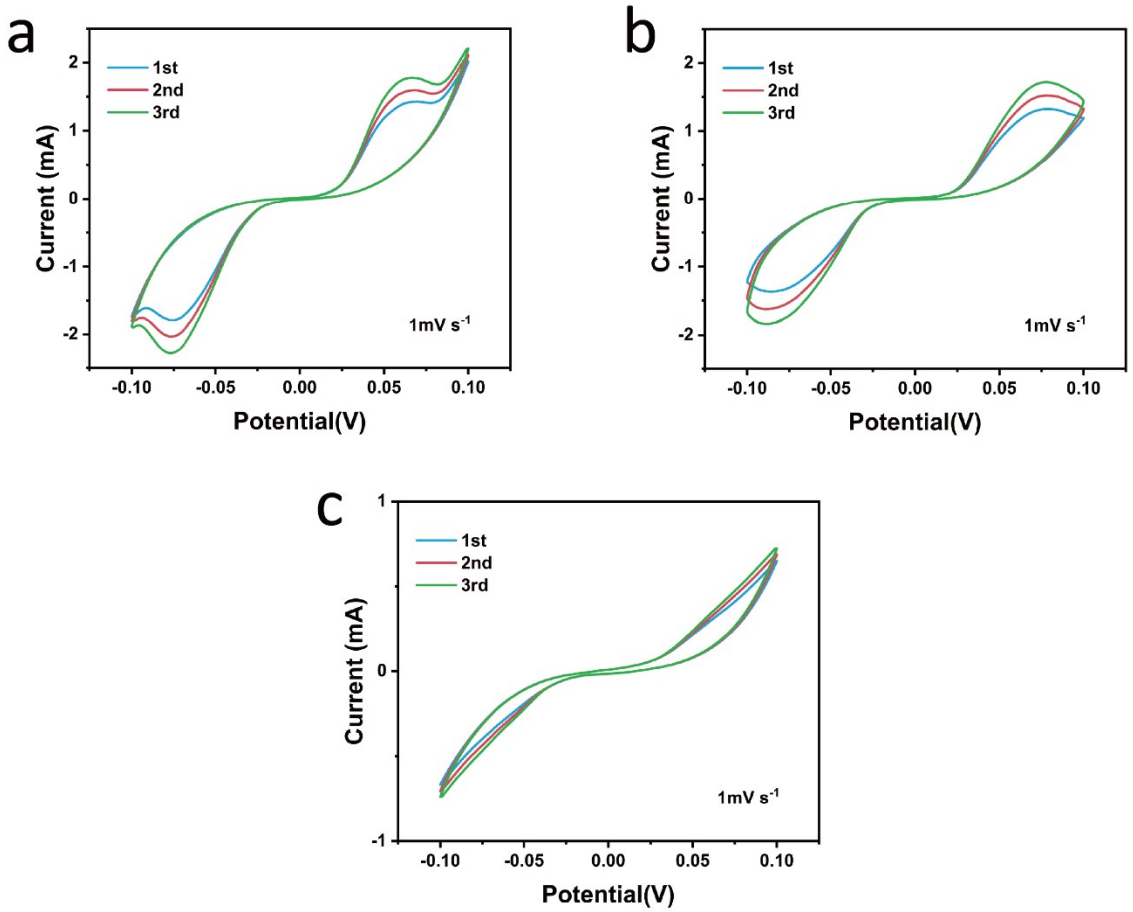

Fig. S12 CV curves of Zn||Zn symmetric cells using (a) GF, (b) GF-B-1, and (c) GF-B-10 separators.

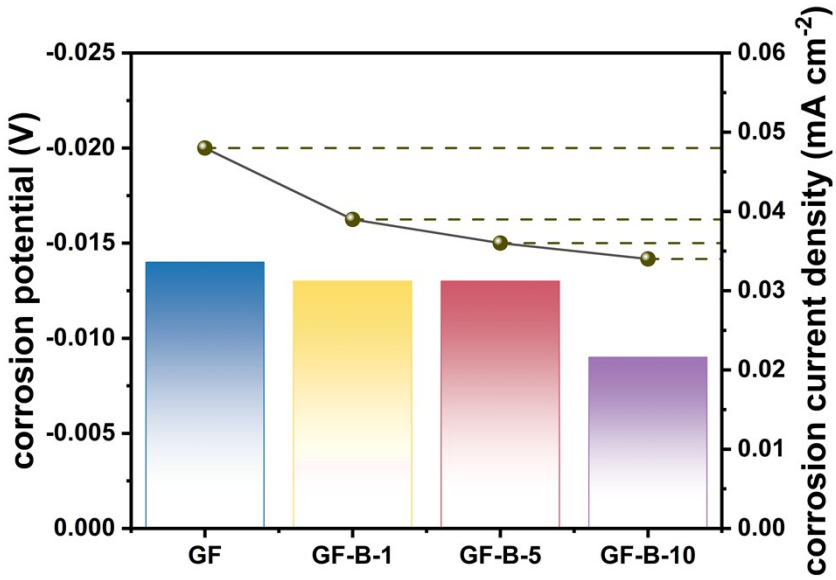

Fig. S13 Corrosion potential, corrosion current density of zinc anodes using GF, GF-B-1, GF-B-5 and GF-B-10 separators.

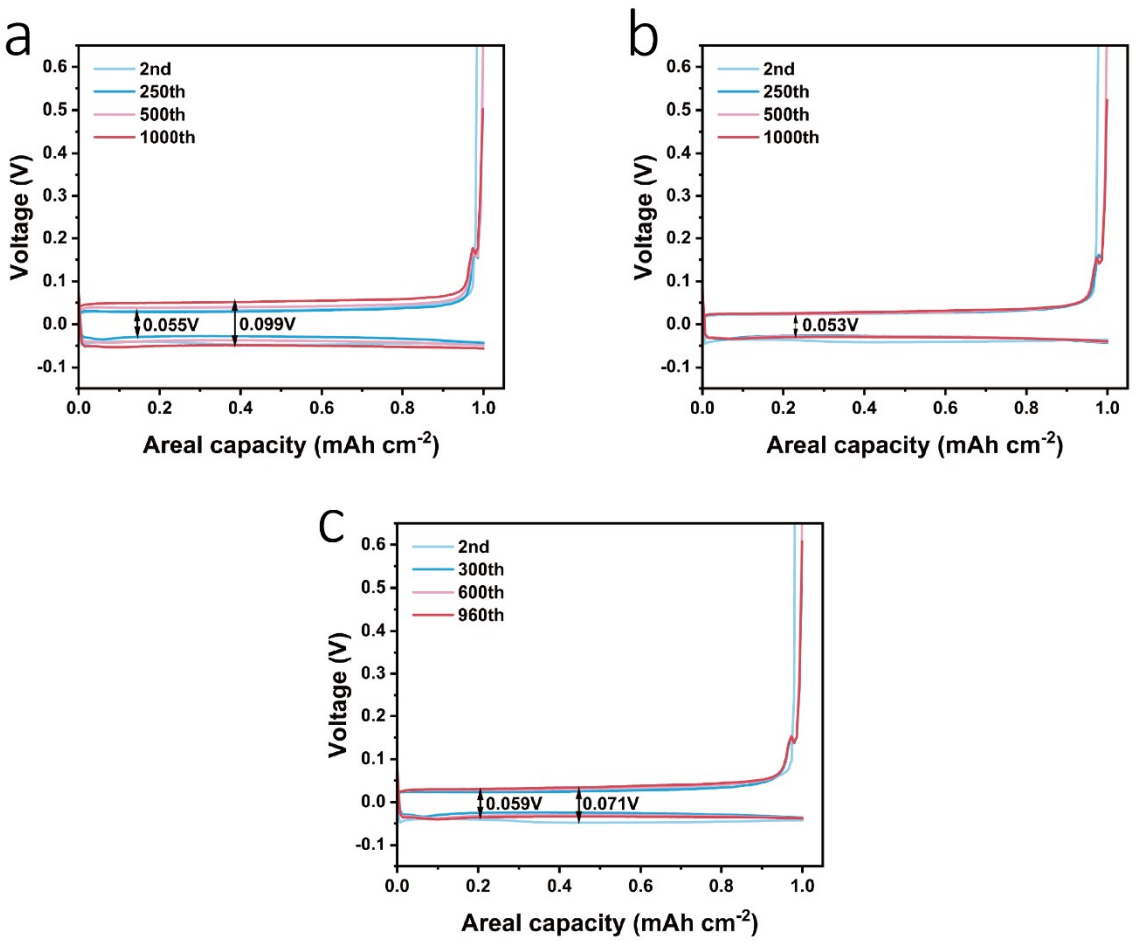

Fig. S14 The voltage profiles of Zn||Cu asymmetric cells with (a) GF, (b) GF-B-1 and (c) GF-B-10 separator.

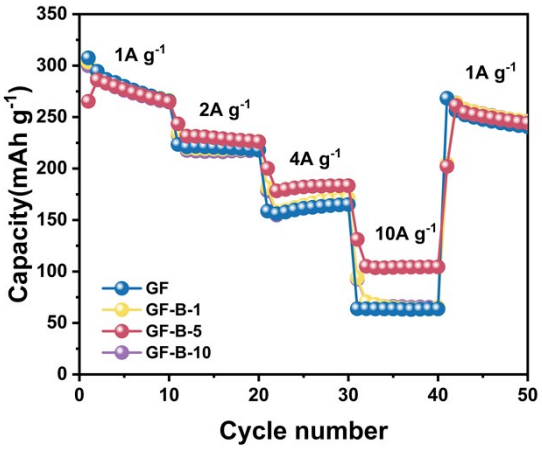

Fig. S15 The rate performance of full cells with GF, GF-B-1, GF-B-5 and GF-B-10 separators.

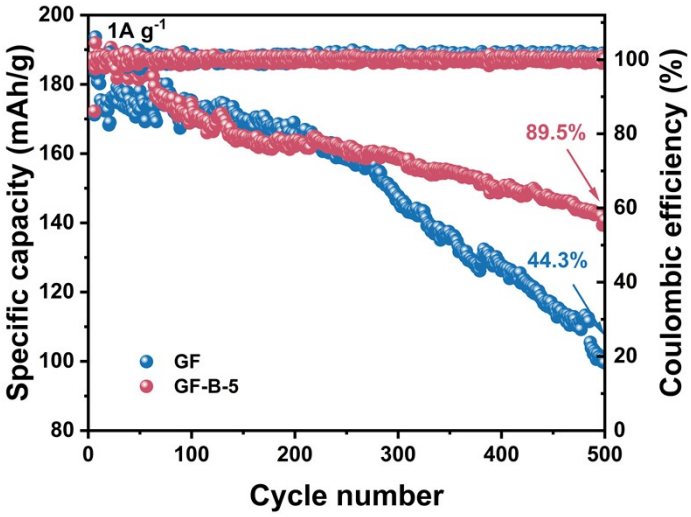

Fig. S16 Cycling performance of Zn||NVO pouch cells with GF and GF-B-5 separators at 1 A g^{-1}.

References

1. K.-F. Zhang, G.-Q. Zhang, X. Liu, Z.-X. Su and H.-L. Li, Journal of Power Sources, 2006, 157, 528-532.

2. Y. Huang, B. Wang, P. Xie, X. Qiu, J. Li, C. Xin, J. Liu and D. Chen, Journal of Energy Storage, 2025, 129, 117395.